J. Fluid Mech. (1997), *vol.* 333, *pp.* 97–123

Structure and energetics of optimal Ekman layer perturbations

By RALPH C. FOSTER

Department of Atmospheric Sciences, Box 351640, University of Washington, Seattle, WA, 98195-1640, USA

(Received 29 August 1995 and in revised form 17 September 1996)

The optimal non-modal perturbations for the neutrally stratified boundary layer in a rotating frame of reference (Ekman layer) are found for a Reynolds number characteristic of the planetary boundary layer (PBL). Two classes of non-modal instabilities are found: evanescent perturbations, with lifetimes up to about one hour, and growing instabilities. The important difference between these types of perturbations is whether or not the optimal non-modal perturbation projects onto an unstable normal mode. The evanescent instabilities are of smaller scale and are oriented at larger angles to the surface isobars compared to either the growing perturbations or normal-mode instabilities. The optimal perturbations take the form of vortices at an acute angle to the geostrophic flow that rapidly transform into streaks with associated overturning motion. The energetics of the optimal perturbations are investigated in detail to clarify the instability mechanism throughout its evolution.

Nonlinear stability analyses of the neutrally stratified Ekman layer have shown that the normal-mode instability will equilibrate with the mean flow to form boundary-layer-scale equilibrium roll eddies aligned closely with the geostrophic flow. However, numerical simulations do not generate these rolls in neutral stratification although they often realize small-scale near-surface streaks oriented at large angles to the geostrophic wind. The evanescent optimal perturbations bear a close resemblance to the simulated streaks. It is proposed that the non-model perturbation mechanism is associated with the streaks.

1. Introduction

In the midlatitudes the portion of the atmospheric planetary boundary layer (PBL) which occupies the region between 10–100 m and 1–2 km above the surface is called the Ekman layer. The classic Ekman profile is an exact solution of the Navier–Stokes equations for the steady three-way balance between the pressure gradient, Coriolis and frictional forces assuming a constant kinematic viscosity. In neutral barotropic conditions the horizontal mean wind forms a logarithmic spiral that has both directional and speed shear, is directed towards low pressure near the surface and is geostrophic (two-way balance between pressure gradient and Coriolis forces) above the boundary layer. The PBL is usually fully turbulent, so the Ekman solution is used as a paradigm mean flow for analytic purposes under the assumption that the Reynolds stresses can be modelled using an eddy viscosity.

Observations, numerical models and theoretical analyses have shown that the Ekman layer frequently contains persistent organized counter-rotating roll vortices that are approximately aligned with the mean wind and span the depth of the boundary

layer is near-neutral to moderately unstably stratified conditions (for details, see the comprehensive reviews by Etling & Brown 1993 and Brown 1980). The spacing between the roll updraughts roughly scales as multiples of the PBL depth (usually double) and is generally 1–5 km. These rolls are coherent structures embedded in the turbulent mean flow which produce an advective and non-local transport of momentum and scalars that mixes the PBL more efficiently than local diffusion. A common interpretation of the action of the quasi-two-dimensional rolls on the PBL is that they form a mean secondary circulation that organizes the smaller-scale fully three-dimensional turbulent eddies into linear patterns. Thus, when rolls are present, the PBL is quite inhomogeneous.

The presence of rolls is often apparent in satellite images of boundary layer 'cloud streets' aligned in rows spaced several kilometres apart that can persist in the downwind direction for hundreds of kilometres and can last for days. Clouds form in the updraught regions between the rolls if the thermodynamic conditions are favourable. However, the rolls are often present in cloud-free conditions as has been demonstrated, for example, in satellite-borne synthetic aperture radar (SAR) images of the sea surface in cloud-free conditions. The SAR image is formed from radar backscatter off the centimetre-scale surface capillary waves which has been empirically related to the wind-driven sea surface stress. Regions of enhanced or reduced surface stress associated with the rolls form linear streaks in the SAR images with orientations and spacings that match those of PBL rolls (Thomson, Liu & Weissman 1983; Gerling 1986; Alpers & Brummer 1994; Mourad & Walter 1996). Coincident SAR and cloud street images show that they are different visualizations of the same phenomena.

Rolls are assumed to be caused by instabilities that form in the PBL and then equilibrate with the mean flow to form a mean secondary circulation (e.g. Faller 1965). Standard linear stability analyses for the constant-eddy-viscosity Ekman layer have been performed for a variety of PBL conditions: for example neutral, barotropic by Lilly (1966) and Leibovich & Lele (1985), stratified by Etling (1971) and stratified baroclinic by Foster (1995). Linear and nonlinear initial value calculations were performed by Faller & Kaylor (1966) and Kaylor & Faller (1972). A consistent picture has emerged from these studies regarding the behaviour of the linear instabilities.

The unstable normal mode in these analyses predicts the roll scale (instability wavelength) and orientation angle relative to the surface isobars fairly well. Unstable stratification tends to decrease the wavelength slightly and to align the rolls more closely with the surface isobars as compared to neutral stratification. Stable stratification tends to increase the angle with the surface isobars. The linear instabilities are damped out in slightly stable stratification. Baroclinic effects produce asymmetric modifications over and above the stratification effects and decrease (increase) the normal mode wavelength in cold (warm) advection and increase (decrease) the orientation angle in cold (warm) advection.

Simple nonlinear analyses by Brown (1970, 1972) and Haack & Shirer (1992) give reasonable predictions of the secondary flow velocities and approximations to the roll-induced modification to the Ekman layer. Faller & Kaylor (1966) and Kaylor & Faller (1972) performed nonlinear integrations of normal-mode perturbations which give better estimates of the equilibrium roll structures. The nonlinear evolution of Ekman layer instabilities has been investigated by Foster (1996). The first 16 Landau coefficients are calculated and stable equilibrium solutions are found to exist for Reynolds number Re at least as high as 1000. Another nonlinear analysis by Mourad & Brown (1990) shows that the perturbation energy can be transferred between scales by interacting resonant triads of instabilities that begin as normal modes. This was

used to explain observations of coincident multiple roll scales in cold air outbreaks. Apparently, normal-mode stability analysis has been quite useful in the study of PBL rolls.

Neutrally stratified low-Re laminar flows in the laboratory agree with the linear analyses up to $Re \sim 200$. At higher Re, equilibrium rolls are seldom realized (Faller & Kaylor 1966). Numerical simulations of higher-Re flows in neutral stratification have also not confirmed the theoretical results. Thus, equilibrium roll circulations are not found in conditions where stability theory predicts they would. However, these simulations often realize transient streaky structures of smaller scale and at larger angles to the surface isobars than those predicted for the rolls. This discrepancy has been the subject of much debate in the field and is a motivation for this paper.

Classical hydrodynamic linear stability theory is based on an eigenvalue (normal-mode) analysis of the linearized equations of motion, the thermodynamic energy equation and the continuity equation and centres on the characteristics of the fastest growing normal mode. A flow is deemed unstable if there exists a normal mode with a positive growth rate for the given mean conditions. In neutral stratification, the basic mean flow parameter is the Reynolds number, Re. The minimum Re for which the flow is unstable is the critical Reynolds number, Re_c. It is assumed that there are fluctuations in nature that will provide an initial perturbation at the wavelength of the most unstable mode which will then proceed to grow faster than any other normal mode and dominate the instability as long as nonlinear effects remain unimportant. Nonlinear effects will either instigate a transition of the flow to disorganized turbulence or allow the perturbation to modify the mean flow enough to create an equilibrium secondary circulation that resembles the unstable normal mode. If the flow is turbulent, this secondary flow is a type of turbulent coherent structure.

Linear theory has been successful in predicting transitions in some fluid systems such as Bénard convection and Taylor–Couette flow. However, the method has failed when applied to certain other canonical solutions such as pressure-driven plane channel (Poiseuille) and circular pipe (Hagen–Poiseuille) flows. Linear stability analysis predicts stability up to $Re_c = 5772$ for plane Poiseuille flow and that pipe flow is linearly stable for all Re. However, experiments have found that plane Poiseuille flow can undergo a transition to turbulence at $Re \sim 1000$ and pipe flow at $Re \sim 2000$.

Recently, non-modal initial perturbations have been shown to have the potential for large transient energy growth compared to modal perturbations for a variety of mean flows (Farrell 1988; Butler & Farrell 1992; Reddy, Schmid & Henningson 1993; Schmid & Henningson 1994). This transient growth provides a possible explanation for observations of 'bypass' transition to turbulence in subcritical plane Poiseuille and Hagen–Poiseuille flows. The non-modal stability analysis is based on the fact that for most flows the linear stability equations are not self-adjoint which means that the eigenfunctions are not orthogonal. We can consider expanding an arbitrary initial perturbation of unit energy using the eigenfunctions (each normalized to have unit energy) as a basis set. Because the basis set is not orthonormal, we will in general have an initial cancellation of contributions between certain combinations of eigenfunctions. If some eigenfunctions are nearly parallel, their expansion coefficients could have relatively large absolute values. However, because the contributions from the different eigenfunctions grow or decay at different rates and have different phase velocities, the initial cancellation of the contributions from nearly parallel eigenfunctions will be removed as time progresses. This could allow transient growth in the energy of the perturbation. This transient growth can occur in subcritical conditions for which no eigenvalue has a positive growth rate. In supercritical conditions, this transient growth

can greatly exceed the exponential growth of the unstable normal mode over a finite time interval.

The non-self-adjoint character of the linear stability equations for the Ekman layer allows transient non-modal perturbations as valid solutions to the system. Normal-mode stability analysis is applicable for asymptotic times while the transient growth occurs at times near zero. If the transient growth is sufficiently large, the flow may become nonlinear before the normal mode has a chance to dominate the solution. This is an important point since study of the PBL rolls and their effect on the mean flow is a nonlinear problem and an initial linear state is needed as a basis for analytic nonlinear analysis. Nonlinear stability analyses assume that the nonlinear effects can be found by expanding around a linear instability that has the same initial shape as the most unstable normal mode (Herbert 1983).

We are left with the following question: Does the most unstable normal mode have time to dominate the instability before nonlinear effects become important? This paper considers the transient growth of optimal perturbations in a neutral barotropic Ekman layer. The optimal perturbation is defined here as the initial condition that achieves the maximum energy norm (to be defined below) at a given time. The optimal perturbations and their temporal development are compared to the unstable normal mode for the same conditions. A subset of the optimal perturbations is found to have the same characteristics as the streaks found in numerical simulations. It is proposed that similar perturbations are associated with the streaks and might inhibit the formation of equilibrium rolls in some situations.

2. Analysis methods

Here we present the equations for the mean and perturbation flows and the relevant non-dimensional parameters. This is followed by an outline of the linear stability problem, the analysis techniques and the numerical methods employed to examine the optimal perturbations. These are included in the body of this paper since the non-normality of the stability operator has important effects on the numerical solutions and because the existence of a continuous spectrum of normal modes complicates the analyses.

2.1. *Ekman layer mean flow*

The Ekman layer solution is used to define the PBL mean flow and its derivation can be found in standard textbooks, e.g. Sorbjan (1989). In a coordinate system aligned with the surface geostrophic wind and non-dimensionalized with the surface geostrophic wind magnitude, G and the Ekman layer e-folding depth, $\delta = (2K/f)^{1/2}$, the horizontal mean flow is

$$U_E = 1 - \mathrm{e}^{-z}\cos z, \tag{2.1}$$

$$V_E = \mathrm{e}^{-z}\sin z, \tag{2.2}$$

where z is the vertical coordinate, K is a constant eddy viscosity, $f = 2\Omega \sin \Lambda$ is the Coriolis parameter, Ω is the rotation rate and Λ is the latitude. The surface geostrophic wind is the fictional wind parallel to the surface isobars that would balance the surface pressure gradient and Coriolis forces. The top of the PBL is at $z \sim 5$. The use of a constant eddy viscosity in the PBL is discussed in Faller (1965), Brown (1981) and Brown & Foster (1994). Faller uses similarity theory to argue that the eddy viscosity in the neutral PBL should be approximately constant. Brown (1981) and Brown & Foster (1994) argue that the use of a constant eddy viscosity for the smaller-scale

turbulent eddies is permissible if an additional 'bookkeeping' of the effects of large-scale eddies such as rolls is included. In this paper, we are implicitly assuming that the eddy viscosity is characteristic of the small-scale turbulent eddies prior to their organization by the larger-scale eddies associated with instabilities of the Ekman layer.

2.2. *Perturbation equations*

The linear stability equations are obtained in the usual manner from the equations of motion and the continuity equation. As discussed in Leibovich & Lele (1985), a scale analysis shows that while the tangential Coriolis force should be omitted in the mean flow equations, it can be significant in the perturbation-scale equations, especially at lower Reynolds numbers. The boundary conditions require all the perturbations to vanish at $z = 0$ and either to vanish or remain bounded as $z \to \infty$. Eigensolutions that vanish as $z \to \infty$ are the discrete normal modes while those that oscillate are elements on the continuous spectrum of normal modes. The perturbation equations are non-dimensionalized using G as the velocity scale, δ as the length scale and $\rho_0 G^2$ as the pressure scale. It can be shown that using a rotational time scale $(2/f)$ yields the same results as for the advective time scale (δ/G). We choose the advective time scale.

The axes of the coordinate system are oriented so that the y-derivative of the perturbations vanishes and the x-axis is directed along the instability wave vector. Several angles need to be defined: ξ is the angle of the surface geostrophic wind from the east, β is the angle of the roll axis from the east and ϵ is angle of the roll axis from the surface geostrophic wind (figure 1*a*). In this coordinate system, the instability wavenumber is $\alpha = (k_x^2 + k_y^2)^{1/2}$ where k_x and k_y are the wavenumbers in the east–west, north–south coordinate system. This rotation is equivalent to Squire's transformation. When the Ekman mean flow is expressed in this coordinate system, a different mean flow profile enters the calculation for each value of ϵ (figure 1*b*). Thus, for each set of mean flow parameters we must survey both α and ϵ when searching for either the fastest growing normal mode or the optimal initial condition.

We assume that the perturbations are of the form

$$u(x, z, t) = \tilde{u}(z, t)\, \mathrm{e}^{\mathrm{i}\alpha x}, \tag{2.3}$$

and the linear perturbation equations are

$$\left[\frac{\partial}{\partial t} + \mathrm{i}\alpha U - \frac{1}{Re}(\mathrm{D}^2 - \alpha^2)\right]\tilde{u} + \tilde{w}U' + \mathrm{i}\alpha\tilde{p} - \frac{1}{Ro}(\tilde{v} + A_1\,\tilde{w}) = 0, \tag{2.4}$$

$$\left[\frac{\partial}{\partial t} + \mathrm{i}\alpha U - \frac{1}{Re}(\mathrm{D}^2 - \alpha^2)\right]\tilde{v} + \tilde{w}V' + \frac{1}{Ro}(\tilde{u} - A_2\,\tilde{w}) = 0, \tag{2.5}$$

$$\left[\frac{\partial}{\partial t} + \mathrm{i}\alpha U - \frac{1}{Re}(\mathrm{D}^2 - \alpha^2)\right]\tilde{w} + \mathrm{D}\tilde{p} + \frac{1}{Ro}(A_1\,\tilde{u} + A_2\,\tilde{v}) = 0, \tag{2.6}$$

$$\mathrm{i}\alpha\tilde{u} + \mathrm{D}\tilde{w} = 0, \tag{2.7}$$

where $A_1 = \sin\beta\cot\Lambda$; $A_2 = \cos\beta\cot\Lambda$, D and primes denote z-derivatives. The following definition is used for the Reynolds number and Rossby number (Ro):

$$Re = \frac{G\delta}{K} = 2\frac{G}{f\delta} = 2Ro. \tag{2.8}$$

Typical values of δ are 100–500 m; Re ranges from 100 to 1000. The terms multiplied by A_1 and A_2 couple the momentum equations through the tangential Coriolis force.

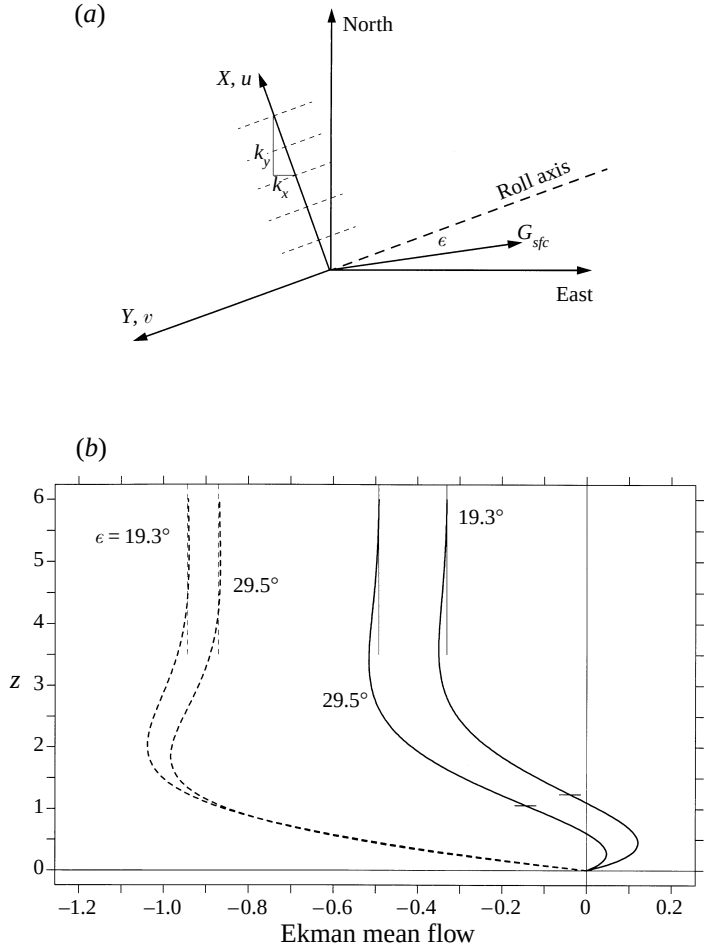

FIGURE 1. (*a*) Coordinate system. (*b*) Ekman layer mean flow for $\epsilon = 29.5°$ and 19.3° corresponding to the optimal perturbations for $\tau = 15$ and 75 respectively. The solid lines are the cross-stream mean flow (U) and the dashed lines are the downstream mean flow (V). The horizontal dashes on the cross-stream velocity mark the inflection point heights. The vertical lines indicate the free-stream geostrophic velocities.

All of the Coriolis couplings are relatively weak compared to the coupling of the overturning (u and w) motions through the perturbation pressure. Thus, the downstream perturbation flow (v) is largely decoupled from the overturning flow. To simplify this analysis we choose $A_1 = A_2 = 0$.

2.3. *Eigenvalue problem*

Pressure can be eliminated from the sixth-order system (2.4)–(2.7) by combining the overturning motion equations (2.4) and (2.6) into an equation for the streamfunction, ψ, where $u = \partial\psi/\partial z$ and $w = -\mathrm{i}\alpha\psi$. The standard linear stability problem assumes that the instabilities are of the separable form $\psi(x, z, t) = \hat{\psi}(z)\,\mathrm{e}^{\lambda t}\,\mathrm{e}^{\mathrm{i}\alpha x}$ where $\lambda = \sigma - \mathrm{i}\omega$ is the eigenvalue. The perturbation grows exponentially with growth rate σ and has frequency ω. The eigenfunction is $\hat{\boldsymbol{q}} = (\hat{\psi}(z), \hat{v}(z))^T$.

Previous eigenvalue studies on the Ekman layer have shown that there are two kinds of instabilities. The 'parallel' mode appears first at $Re \sim 54$ (if the tangential Coriolis

force is omitted). This mode is oriented at $\epsilon \sim -15°$ (towards high pressure) and extracts its energy from the downstream shear production terms and couples it into the overturning motion through the Coriolis terms. Because the Coriolis coupling scales as Re^{-1} no apparent peak in contours of the growth rate associated with this mode can be seen when $Re \sim 200$ because of the emergence at $Re \sim 113$ of a much faster growing instability, the 'inflection point' mode which has been associated with the PBL rolls. This mode extracts its energy from the cross-stream shear production and occurs at $\epsilon \sim 15°$–$20°$ with $\alpha \sim 0.5$.

2.4. *Non-modal instabilities*

The theory for non-modal instabilities has been presented rigorously by Farrell (1988); Butler & Farrell (1992); Reddy & Henningson (1993); Reddy *et al.* (1993); and Schmid & Henningson (1994). Central to these theories is the definition of the size or norm of the instability which must incorporate contributions from all components of the solution. For this analysis we choose the kinetic energy norm to measure the perturbation growth.

The eigenfunction expansion technique described in Schmid & Henningson (1994) is applied. Special attention is paid to the difficulties associated with the contributions from the continuous spectrum of normal modes which were not part of previous studies. We assume that any solution, $\boldsymbol{q}$, to the system of equations (2.4)–(2.7) can be written as an eigenfunction expansion:

$$\boldsymbol{q}(x,z,t) = \begin{bmatrix} \psi \\ v \end{bmatrix} = \mathrm{e}^{\mathrm{i}\alpha x} \sum_{n=1}^{N} k_n(t) \begin{bmatrix} \hat{\psi}(z) \\ \hat{v}(z) \end{bmatrix}_n = \mathrm{e}^{\mathrm{i}\alpha x} \sum_{n=1}^{N} k_n(t)\, \hat{\boldsymbol{q}}_n(z), \tag{2.9}$$

in which the eigenfunctions are ordered in terms of decreasing growth rate, σ_n, and the solution is completely determined by the vector of expansion coefficients, $\boldsymbol{k}$. The value of N remains to be determined.

There is a finite number of discrete normal modes and a continuous spectrum of normal modes for the Ekman layer stability problem. An exact solution would require N to equal the number of discrete normal modes and an additional integral over the continuous spectrum would need to be included. The spectral numerical solution finds a finite number of eigenfunctions. Some of these are the discrete normal modes but the majority are discrete representations of elements of the continuous spectrum. The normal modes on the continuous spectrum have negligible contributions in the high-shear regions near the surface and are most significant above the PBL. As in the analysis of the Blasius boundary layer described in Butler & Farrell (1992) we assume that the optimal perturbations will be mainly composed of contributions from the discrete normal modes which are mainly significant in the PBL. We can treat the discrete representations of the continuous spectrum as if they are discrete normal modes and include them in the summation. Thus, N will be determined by numerical experimentation varying the spectral resolution used to solve the eigenvalue problem and the range of growth rates included in the eigenfunction expansion (2.9). Previous studies (Schmid & Henningson 1994 and Reddy *et al.* 1993) have found that N can be much less than the number of eigenfunctions in the linear stability solution, which results in a substantial decrease in the computer time required to perform the non-modal analysis. In what follows we will not distinguish between the exact equations and their discrete approximations. This relationship is explored in Reddy *et al.* (1993) and Schmid & Henningson (1994).

2.4.1. *Energy and amplitude norms*

We define an inner product $(\boldsymbol{q}_i, \boldsymbol{q}_j) = \int_0^\infty \boldsymbol{q}_j{}^\dagger \boldsymbol{q}_i \, \mathrm{d}z$ where the † superscript denotes the Hermitian adjoint (complex conjugate transpose). The amplitude or 2-norm of $\boldsymbol{q}$ is the square-root of the inner product of $\boldsymbol{q}$ with itself and measures the amplitude of the instability:

$$(\boldsymbol{q}, \boldsymbol{q}) = \|\boldsymbol{q}\|_2^2 = \int_0^\infty [|\psi|^2 + |v|^2] \, \mathrm{d}z. \tag{2.10}$$

Similarly, the energy norm is defined as

$$\|\boldsymbol{q}\|_E^2 = \int_0^\infty (|\psi_z|^2 + \alpha^2 |\psi|^2 + |v|^2) \, \mathrm{d}z, \tag{2.11}$$

where the definition of the energy inner product is

$$(\boldsymbol{q}_i, \boldsymbol{q}_j)_E = \int_0^\infty \left(\frac{\partial \psi_j^\dagger}{\partial z} \frac{\partial \psi_i}{\partial z} + \alpha^2 \psi_j{}^\dagger \psi_i + v_j{}^\dagger v_j \right) \mathrm{d}z. \tag{2.12}$$

The eigenfunction expansion (2.9) (with the eigenfunctions normalized to have unit energy norm) may be combined with (2.11) and (2.12) to give an expression for the energy norm of a perturbation:

$$\|\boldsymbol{q}\|_E^2 = (\boldsymbol{q}, \boldsymbol{q})_E^2 = \int_0^\infty \sum_m^N k_m{}^\dagger \sum_n^N k_n \left[\frac{\partial \hat{\psi}_m^\dagger}{\partial z} \frac{\partial \hat{\psi}_n}{\partial z} + \alpha^2 \hat{\psi}_m{}^\dagger \hat{\psi}_n + \hat{v}_m{}^\dagger \hat{v}_n \right] \mathrm{d}z. \tag{2.13}$$

This may be written in matrix form as

$$\|\boldsymbol{q}\|_E^2 = \boldsymbol{k}^\dagger \boldsymbol{M} \boldsymbol{k}, \tag{2.14}$$

where $\boldsymbol{M}$ is the $N \times N$ positive definite Hermitian matrix (with ones along the diagonal) whose elements are constructed from the energy inner products between the normalized eigenfunctions:

$$M_{mn} = \int_0^\infty \left[\frac{\partial \hat{\psi}_m^\dagger}{\partial z} \frac{\partial \hat{\psi}_n}{\partial z} + \alpha^2 \hat{\psi}_m{}^\dagger \hat{\psi}_n + \hat{v}_m{}^\dagger \hat{v}_n \right] \mathrm{d}z. \tag{2.15}$$

Note that if the stability problem was self-adjoint, $\boldsymbol{M}$ would be the identity matrix. Any positive definite Hermitian matrix has an $N \times N$ matrix square root, $\boldsymbol{F}$, defined as $\boldsymbol{F}^\dagger \boldsymbol{F} = \boldsymbol{M}$. This allows us to relate the energy norm of $\boldsymbol{q}$ to its related 2-norm as follows:

$$\|\boldsymbol{q}\|_E^2 = \boldsymbol{k}^\dagger \boldsymbol{M} \boldsymbol{k} = \boldsymbol{k}^\dagger \boldsymbol{F}^\dagger \boldsymbol{F} \boldsymbol{k} = \|\boldsymbol{F}\boldsymbol{k}\|_2^2. \tag{2.16}$$

It is straightforward to extend the definition of an energy norm from vectors to matrices. The 2-norm of a matrix, $\boldsymbol{A}$, is the maximum possible relative increase in amplitude of any non-zero vector, $\boldsymbol{x}$, that $\boldsymbol{A}$ multiplies: $\|\boldsymbol{A}\|_2 = \mathrm{Max} \, \|\boldsymbol{A}\boldsymbol{x}\|_2 / \|\boldsymbol{x}\|_2$. Similarly, we define the energy norm of $\boldsymbol{A}$ as the maximum possible relative increase in energy of any non-zero vector and use (2.16) to relate the matrix energy norm to the matrix amplitude norm:

$$\|\boldsymbol{A}\|_E = \mathrm{Max} \frac{\|\boldsymbol{A}\boldsymbol{x}\|_E}{\|\boldsymbol{x}\|_E} = \mathrm{Max} \frac{\|\boldsymbol{F}\boldsymbol{A}\boldsymbol{x}\|_2}{\|\boldsymbol{F}\boldsymbol{x}\|_2} = \mathrm{Max} \frac{\|\boldsymbol{F}\boldsymbol{A}\boldsymbol{F}^{-1}\boldsymbol{F}\boldsymbol{x}\|_2}{\|\boldsymbol{F}\boldsymbol{x}\|_2} = \|\boldsymbol{F}\boldsymbol{A}\boldsymbol{F}^{-1}\|_2. \tag{2.17}$$

The amplitude norm of a matrix is computationally useful since it can be found using singular value decomposition (SVD) which is available in standard linear algebra software packages.

2.4.2. *Transient growth*

It is possible to rewrite the system of equations (2.4)–(2.7) in matrix form to get the general system of differential equations:

$$\frac{\partial \boldsymbol{q}}{\partial t} = \boldsymbol{C}\boldsymbol{q}, \tag{2.18}$$

where $\boldsymbol{C}$ is the matrix representation of the spatial terms in (2.4)–(2.7). The linear stability (eigenvalue) problem may then be written as

$$\boldsymbol{C}\hat{\boldsymbol{Q}} = \hat{\boldsymbol{Q}}\boldsymbol{\Lambda}, \tag{2.19}$$

where $\boldsymbol{Q}$ is the matrix with the eigenvectors as columns and $\boldsymbol{\Lambda} = \mathrm{diag}\,(\lambda_1, \lambda_2, \ldots, \lambda_N)$ is the diagonal matrix of eigenvalues sorted by decreasing growth rate. If we substitute the eigenfunction expansion (2.9) and (2.19) into (2.18) we find:

$$\boldsymbol{k} = \mathrm{e}^{\boldsymbol{\Lambda} t}\boldsymbol{k}_0, \tag{2.20}$$

where $\boldsymbol{k}_0$ is the vector of expansion coefficients that defines the initial perturbation.

Equation (2.20) is an expression for the evolution of arbitrary disturbances. The contribution of each eigenfunction, $\hat{\boldsymbol{q}}_j$, to the solution grows from its initial value, given by k_{0j}, at its normal-mode growth rate, σ_j. The fastest growing discrete normal mode will determine the evolution at late times. The transient growth occurs because the initial cancellation of contributions between the non-orthogonal eigenfunctions is lost as the expansion coefficients grow or decay at different rates and propagate at different velocities. We have already assumed that the initial condition has unit energy norm. Thus, the maximum possible transient energy growth in the perturbation at any time is given by

$$\|\mathrm{e}^{\boldsymbol{\Lambda} t}\|_E = \|\boldsymbol{F}\mathrm{e}^{\boldsymbol{\Lambda} t}\boldsymbol{F}^{-1}\|_2 = \|\boldsymbol{F}\,\mathrm{diag}\,\{\mathrm{e}^{\lambda_1 t}, \mathrm{e}^{\lambda_2 t}, \ldots, \mathrm{e}^{\lambda_N t}\}\,\boldsymbol{F}^{-1}\|_2. \tag{2.21}$$

For any time, τ, the energy norm given by (2.21) corresponds to a unique initial condition which we call the optimal perturbation. No other initial condition can result in a larger energy norm at $t = \tau$; however, the optimal perturbation may either grow or decay when $t > \tau$. The locus of energy norms from a range of τ values defines the boundary of possible energy growth from arbitrary initial conditions of unit energy.

According to (2.21) we find the energy norm of the perturbation by calculating the 2-norm of the diagonal growth matrix scaled by the matrix $\boldsymbol{F}$. The 2-norm of a matrix is its principal singular value (Golub & van Loan 1983). The optimal initial condition is related to the right-hand principal singular vector as follows. The SVD of the energy growth operator in (2.21) is

$$\boldsymbol{F}\mathrm{e}^{\boldsymbol{\Lambda} t}\boldsymbol{F}^{-1} = \boldsymbol{U}\boldsymbol{S}\boldsymbol{V}^{\dagger}, \tag{2.22}$$

where $\boldsymbol{U}$ and $\boldsymbol{V}$ are unitary matrices and $\boldsymbol{S}$ is the diagonal matrix of singular values. The principal singular value is $S_{11} = s_1$, and the principal left- and right-hand singular vectors are the first columns of $\boldsymbol{U}$ and $\boldsymbol{V}$, respectively, $\boldsymbol{u}_1$ and $\boldsymbol{v}_1$. Thus, the relationship between s_1, $\boldsymbol{u}_1$ and $\boldsymbol{v}_1$ is

$$\boldsymbol{F}\mathrm{e}^{\boldsymbol{\Lambda} t}\boldsymbol{F}^{-1}\boldsymbol{v}_1 = s_1\,\boldsymbol{u}_1. \tag{2.23}$$

Equation (2.23) shows that the energy growth operator maps the vector $\boldsymbol{v}_1$ onto the output vector $\boldsymbol{u}_1$ and amplifies it by the factor s_1. The optimal initial condition, $\boldsymbol{v}_1$, can

be related to the eigenfunction expansion coefficients by comparing (2.20) and (2.23) to get

$$\boldsymbol{k}_0 = \boldsymbol{F}^{-1}\boldsymbol{v}_1. \tag{2.24}$$

2.5. *Numerical method*

A solution for the optimal perturbation requires a solution to the eigenvalue problem (2.4)–(2.7) which is then used to construct the matrix $\boldsymbol{M}$ (2.15) and its square-root, $\boldsymbol{F}$, from the normalized eigenfunctions and the matrix $\exp(\boldsymbol{\Lambda} t)$ from the eigenvalues. The spectral/Galerkin method described in Spalart, Moser & Rogers (1991) is used to discretize the spatial terms in these equations. The non-divergent spectral basis functions are linear combinations of Jacobi polynomials in the variable $\exp(-z/z_0)$ that exactly satisfy the homogeneous boundary conditions at $z = 0$ and as $z \to \infty$. The inner products in the Galerkin method are solved using Gaussian quadrature. The parameter z_0 controls the height below which the basis functions have a significant contribution. Tuning this numerical method requires finding values for z_0, N_{poly} (maximum order of the polynomials in the spectral expansion) and σ_{min} (minimum growth rate of the eigenfunctions included in the eigenfunction expansion (2.9)) that give sufficiently accurate solutions. The method finds $2(N_{poly}+1)$ eigenvalues in neutral stratification. Numerical experimentation determined that $z_0 = 3.1$ resulted in well-converged eigenvalues for the discrete normal modes over a wide range of N_{poly} in typical conditions.

This spectral method is very efficient at calculating the discrete normal modes, but does a much poorer job at resolving the continuous spectrum. This is partly because the basis functions have little or no resolution above the boundary layer, which is where the continuous spectrum modes are the most significant, and partly due to the non-normality of the stability operator. Using the method of Grosch & Salwen (1978), the phase speed of the continuous spectrum for the neutral barotropic Ekman layer may be found by solving the following third-order polynomial for χ:

$$\chi\left[\chi^2 - \frac{(b+\alpha A_2)^2}{\alpha^2 Ro^2 (b^2+\alpha^2)}\right] = 0 \tag{2.25}$$

in which b is a real parameter that ranges between $-\infty$ and $+\infty$. The phase speed of the continuous spectrum is related to χ by

$$c = \frac{\mathrm{i}\lambda}{\alpha} = \chi + U_\infty + \frac{1}{\mathrm{i}\alpha\, Re}(b^2+\alpha^2), \tag{2.26}$$

where $U_\infty = \lim_{z\to\infty} U(z)$. In neutrally stratified barotropic conditions and with the tangential Coriolis force omitted, the continuous spectrum is entirely in the stable half-plane along two branches centred around $-\mathrm{i}\alpha U_\infty$.

Eigenvalues for the typical conditions of $\alpha = 0.5$, $\epsilon = 20°$ and $Re = 500$ for neutrally stratified, barotropic conditions omitting the tangential Coriolis force are shown in figure 2 for $N_{poly} = 200$, 120 and 60. Fourteen discrete normal modes are resolved when $N_{poly} = 200$. They occur in two branches, one that splits off the continuous spectrum at $\sigma \approx -0.17$ and extends towards more negative frequency and larger growth rates. The unstable eigenvalue represents the inflection-point instability. The discrete modes on the other branch have small negative real parts and are very close to the continuous spectrum. These are associated with the second cross-stream inflection point above the surface in the Ekman spiral. All three spectral resolutions agree very closely for all of the discrete eigenvalues except for the ones approximately at $-0.166 + 0.137\mathrm{i}$ (which is only resolved when $N_{poly} = 200$) and $-0.008\,14 + 0.169\mathrm{i}$.

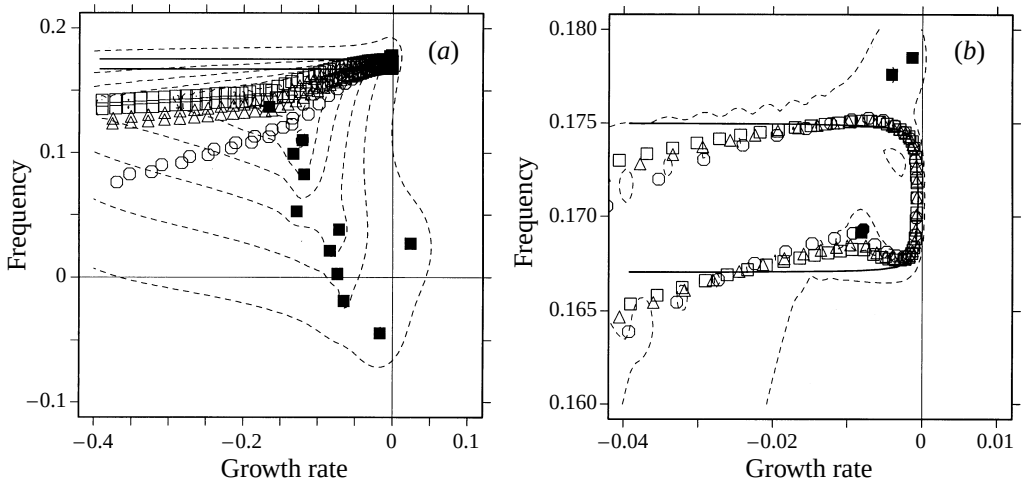

FIGURE 2. (*a*) Effect of resolution on the eigenvalues for the conditions $\alpha = 0.5$, $\epsilon = 20°$, $Re = 500$, neutrally stratified, barotropic and no tangential Coriolis force for $N_{poly} = 200$ (squares), 120 (triangles) and 60 (circles). Filled symbols are discrete normal modes and hollow symbols are discrete representations of elements on the continuous spectrum. (*b*) Expanded view near the continuous spectrum. In both (*a*) and (*b*) the predicted behaviour of the continuous spectrum is plotted as solid lines. Contours of the ϵ-pseudospectrum are plotted as dashed lines. In (*a*) the contours change by factors of 10 from 10^{-7} (inner) to 10^{-2} (outer). In (*b*) only the 10^{-3} and 10^{-4} contours are shown.

These two modes are very close to where the discrete modes approach the continuous spectrum. The numerical continuous modes agree well with the exact solution when $\sigma > -0.01$ but diverge significantly at lower growth rates.

The non-normality of the Ekman layer stability operator exacerbates the problem of resolving the continuous spectrum and the discrete normal modes that are near the separation point. This effect is best understood by analysing the ϵ-pseudospectrum, an extension of eigenvalue analysis developed by Trefethen (1992) and Trefethen *et al.* (1993) that is useful for describing the behaviour of non-normal operators. Schmid & Henningson (1994) and Reddy *et al.* (1993) have applied this technique in hydrodynamic stability problems to explain the behaviour of the numerical solutions and as a theoretical tool for exploring the transient growth. An ϵ-pseudoeigenvalue of a matrix, $\boldsymbol{C}$, is the set of complex numbers, z, such that $\|(z\boldsymbol{I}-\boldsymbol{C})^{-1}\|_E \geqslant \epsilon^{-1}$. In this case $\boldsymbol{C}$ is the discrete matrix representation of the operator in (2.18). The spectrum of $\boldsymbol{C}$ corresponds to the ϵ-pseudospectrum with $\epsilon = 0$. The ϵ-pseudospectra are nested regions in the complex plane. Normal operators have ϵ-pseudospectrum contours that form circles of radius ϵ around the eigenvalues. Contours of the ϵ-pseudospectrum calculated with $N_{poly} = 200$ are included in figure 2. The high sensitivity to small errors is apparent where the main branch of discrete eigenvalues separates from the continuous spectrum. The eigenfunctions corresponding to these eigenvalues are nearly parallel. This non-normality of the operator contributes to the numerical error in resolving the continuous spectrum and the nearby discrete modes.

To determine N_{poly} and σ_{min} the solutions to the maximum energy growth equation (2.21) were calculated for different time intervals, τ, over a wide range of N_{poly} and σ_{min}. The energy norm calculation must include all of the resolved discrete normal modes in order to converge. When σ_{min} is about twice the growth rate where the discrete modes separate from the continuous spectrum ($\sigma_{min} = -0.4$ for the conditions in figure 2) the energy norms agree to a relative error of about 0.01 % for N_{poly} ranging

between 40 and 200. The number of eigenfunctions, N, included in the expansion (2.9) is slightly greater than N_{poly}, about half the total number found. Since the operations to set up the matrices and to find the SVD or $O(N^2)$ and $O(N^3)$ this is a substantial reduction in computer time.

The serious question remains of whether or not the spectral model's representation of the continuous spectrum modes is adequate. As expected from figure 2 the largest absolute values of the expansion coefficients in the optimal initial condition (2.24) come from the modes nearest to the point where the discrete modes separate from the continuous spectrum and it is the loss of cancellation between these modes that leads to the transient growth. The absolute values of the expansion coefficients for the discrete modes generally stand out clearly from the contributions from the continuous spectrum. These results suggest that good resolution of the discrete normal modes is necessary but that resolving the continuous spectrum is not critical in calculating the transient growth. This would be expected on physical grounds since the continuous spectrum is required mathematically to represent the susceptibility of the PBL to perturbations above the boundary layer, whereas we are concerned with perturbations that grow within the PBL. These perturbations should be concentrated near the surface in order to extract energy from the high-shear region.

To verify this, a second spectral/Galerkin numerical model was constructed that uses linear combinations of Chebyshev polynomials as basis functions that exactly satisfy the continuity equation and the boundary condition at $z = 0$ (Leibovich & Lele 1985). These polynomials also satisfy the condition that all perturbations vanish at a finite height, z_{top}, above the surface. Good results were found when $z_{top} = 40$. Compared to the Spalart *et al.* (1991) method, about twice as many polynomials must be included to converge the discrete normal modes to the same precision. Because these basis functions have equal resolution in the lower and upper halves of the domain, the numerical and theoretical continuous spectra agree to lower growth rates using this method as compared to the Spalart *et al.* (1991) method. However, most of the continuous spectrum modes that are found numerically have high growth rates so the number of eigenfunctions that must be included in (2.9) is quite large. The calculated energy norms using the Leibovich & Lele (1985) method agree well with the Spalart *et al.* (1991) method, but take significantly more computer time to calculate.

All calculations below were performed in 64-bit precision with $N_{poly} = 80$, $z_0 = 3.1$ and with σ_{min} set approximately to twice the growth rate where the discrete modes separate from the continuous spectrum. The linear algebra calculations were performed using LAPACK (Anderson *et al.* 1992) and MATLAB (1992) routines.

3. Structure of the optimal Ekman layer perturbations

We examine the typical condition of $Re = 500$ and omit the tangential Coriolis force. Results for other Re are qualitatively similar. Interpreting these results can be simplified by choosing magnitudes for G, δ and K that are characteristic of the PBL. For the typical midlatitude value of $f = 10^4\,\mathrm{s}^{-1}$, one non-dimensional time unit is equal to 40 s. If we further assume that $\delta = 320$ m, then $G = 8\ \mathrm{m\ s}^{-1}$ and $K = 5\ \mathrm{m}^2\ \mathrm{s}^{-1}$. We first discuss the wavenumber and orientation angle dependence and the size of the optimal perturbations and then examine the evolution of their shapes.

3.1. *Optimal perturbation dependence on wavenumber and orientation*

The dependence of the linear (normal mode) instability growth rate on α and ϵ is shown in figure 3. The most unstable discrete normal mode occurs at $\alpha = 0.5$ and $\epsilon = 17°$ and

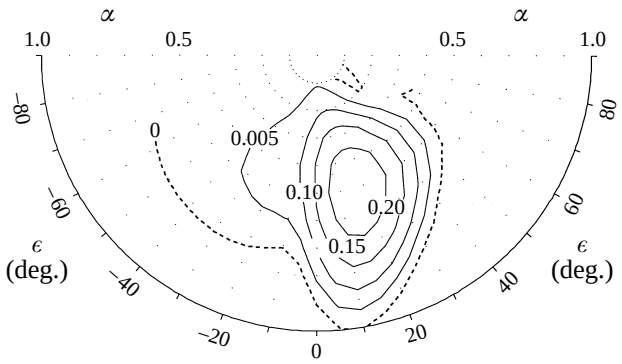

FIGURE 3. Contour plot of the linear growth rate for $Re = 500$ and $Ri = 0$ as a function of wavenumber, α, and orientation angle, ϵ. The maximum growth rate of 0.0239937 occurs at $\alpha = 0.5$ and $\epsilon = 17°$. The contour interval is 0.005.

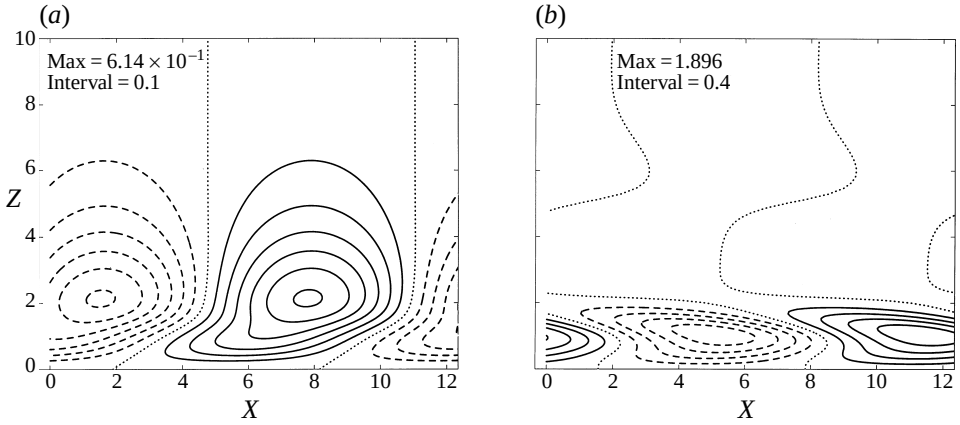

FIGURE 4. Eigenfunction corresponding to the most unstable normal mode for $Re = 500$, $\alpha = 0.5$, $\epsilon = 17°$. (*a*) Streamfunction, ψ; (*b*) downstream velocity, v. The eigenfunction has been normalized to have unit energy norm.

has a growth rate of about 0.024 which corresponds to an e-folding time of about 28 min. Similar results are found for most high Re; e.g. when $Re = 1000$, the growth rate is about 0.028, α remains at 0.5 and $\epsilon = 16°$. Typical roll perturbation velocities are on the order of 1 m s^{-1} so an estimate of the eddy turnover time of a PBL roll is 20–50 min (30–75 non-dimensional time units). Thus, the linear instability e-folding time and PBL roll turnover times are quite similar. The eigenfunction for the most unstable discrete normal mode is shown in figure 4.

The maximum possible energy norm as a function of α and ϵ is plotted in figure 5 for $\tau = 15$, 25, 50 and 100, where τ is the time for which the perturbation is optimal. Similar calculations were performed for a range of τ and the results are summarized in table 1(*a*). Additional results for $Re = 150$ and 1000 are given in tables 1(*b*) and 1(*c*). The $\tau = 100$ optimal energy norm contours are similar to the linear growth rate contours of figure 3 and the maximum occurs in the region where the system is linearly unstable. The $\tau = 50$ maximum also occurs in the region where the system is linearly unstable, but the contours do not have the same shape as in figure 3. The $\tau = 15$ and

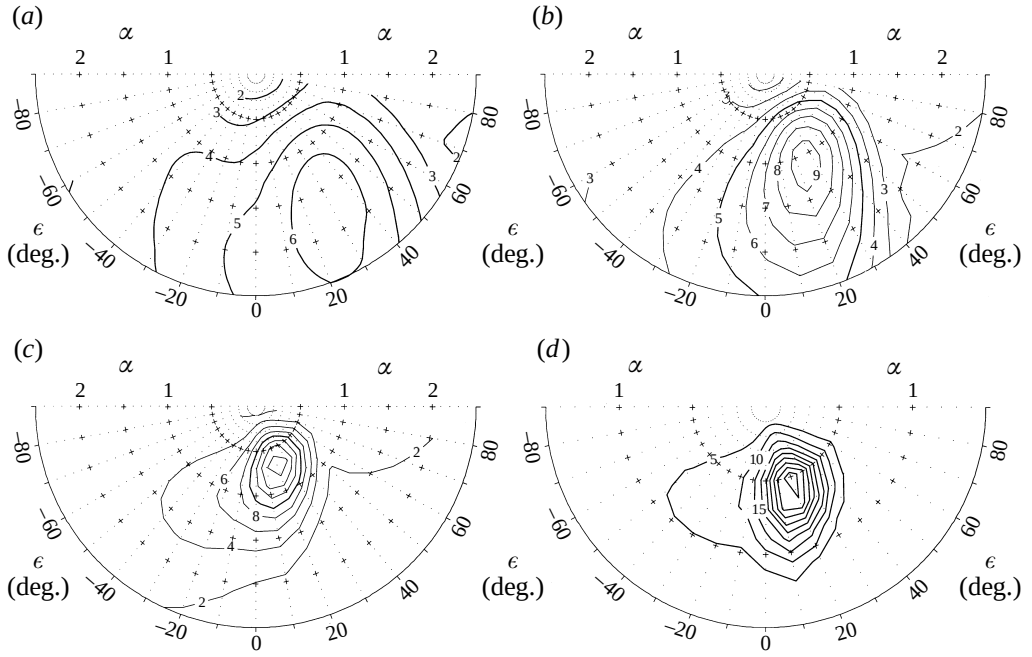

FIGURE 5. Contour plots of the maximum possible energy norm for $Re = 500$ as a function of wavenumber, α, and orientation angle, ϵ for time intervals (*a*) $\tau = 15$; (*b*) $\tau = 25$; (*c*) $\tau = 50$; (*d*) $\tau = 100$. The contour interval is 1 in (*a*) and (*b*); 2 in (*c*) and 5 in (*d*).

25 energy growth occurs over a wider range of wavenumbers and orientation angles and the peak energy norms occur at $\alpha = 1.700$ and $\epsilon = 29.5°$ and $\alpha = 1.085$ and $\epsilon = 25.3°$ respectively, conditions where the system is linearly stable.

The change in wavenumber and orientation angle for the optimal perturbations and the corresponding maximum energy norms are shown in figure 6. The wavelength and orientation of the optimal perturbations asymptote slowly to those of the normal-mode instability at the longer time intervals ($\tau > 30$). Smaller-scale perturbations that are oriented at larger angles to the surface isobars can extract energy from the mean flow when $\tau < 30$ although this growth is evanescent. These evanescent instabilities have not been previously identified as solutions to the Ekman layer perturbation equations.

The individual energy growth rate curves for the optimal non-modal perturbations as functions of time for $\tau = 5$, 10, 15 and 25 – all with wavenumbers greater than one – continue to increase for a short time after their respective τ values before eventually decaying. The individual growth rates for $\tau = 35$, 50 and 75 asymptotically grow at the different growth rates of the unstable normal modes for their respective wavenumbers and orientation angles.

Included on figure 6(*c*) is the maximum possible energy growth corresponding to non-nodal perturbations with the same wavenumber and orientation angle as the linearly most unstable mode. This curve remains below the optimal energy growth curve out to $\tau = 500$, although the two curves must coincide as $\tau \to \infty$. The energy norms of the overall optimal perturbations are no more than a factor of 2 larger than the optimal perturbations constrained to $\alpha = 0.5$, $\epsilon = 17°$. All optimal perturbations with these α and ϵ project onto the unstable normal mode and so they grow asymptotically at its growth rate. All of these perturbations begin to be dominated by the unstable normal mode when $t > \sim 40$ (the reciprocal of its growth rate). At later

	τ	α_c	ϵ_c ± 0.1 deg.	Energy norm	Growth rate, unstable DNM	Energy norm
(*a*)		± 0.005				$\alpha = 0.5$, $\epsilon = 17°$
	5	3.445	39.2	2.97874	—	1.55508
	10	2.305	33.8	4.93420	—	2.27228
	15	1.700	29.5	6.60247	—	3.13364
	25	1.085	25.3	9.60176	—	5.34806
	35	0.850	22.9	12.6456	0.00280876	8.29071
	50	0.695	20.7	17.8085	0.01733662	14.0031
	75	0.605	19.3	30.1910	0.02206721	27.0394
	100	0.580	18.5	53.0331	0.02295095	48.6338
	125	0.560	18.1	95.3022	0.02343000	88.6443
	150	0.550	17.8	171.580	0.02362438	161.986
	200	0.540	17.5	561.257	0.02377725	537.218
	250	0.530	17.4	1848.85	0.02387968	1783.32
	300	0.525	17.3	6106.30	0.02392098	5918.83
	400	0.520	17.2	66882.4	0.02395334	65203.5
	500	0.520	17.1	734009	0.02395633	718297
(*b*)		± 0.005				$\alpha = 0.54$, $\epsilon = 9.7°$
	5	2.12	20.5	2.03439	—	1.43296
	10	1.555	20.5	2.89329	—	1.92278
	15	1.23	18	3.55980	—	2.43821
	20	1.03	15.5	4.09629	—	2.97279
	25	0.895	14	4.54591	—	3.51778
	30	0.805	12.5	4.93363	—	4.05886
	35	0.745	11.5	5.27575	0.0022817	4.57993
	60	0.620	9.4	6.12599	0.0068217	5.90277
	75	0.530	7.6	7.26428	0.0075542	7.22897
	100	0.505	7.5	8.29903	0.0074165	8.25995
(*c*)		± 0.025				$\alpha = 0.5$, $\epsilon = 16°$
	5	4.475	46.2	3.57837	—	1.60864
	10	2.91	39.5	6.28062	—	2.41380
	15	2.06	34.5	8.62217	—	3.39657
	20	1.54	31.5	10.7672	—	4.58141
	25	1.24	29.5	12.9192	—	6.00634
	35	0.92	27.0	17.6364	—	9.71165
	50	0.73	24.5	26.3732	0.016040	17.7529
	75	0.62	22.0	49.0778	0.024547	39.3197
	100	0.59	20.5	93.4781	0.026195	78.6567
	125	0.57	20.0	182.727	0.026852	156.927

TABLE 1. Dependence of the optimal initial condition on wavenumber, α, and orientation angle, ϵ, as a function of time interval, τ, in neutral stratification and barotropic conditions. The energy norm for each optimal is given in the fourth column, the growth rate of the unstable discrete normal mode for the growing perturbations in the fifth column, and the energy norm for optimal non-modal perturbations constrained to conditions of the most unstable normal mode in the sixth column. (*a*) $Re = 500$, (*b*) $Re = 150$, (*c*) $Re = 1000$.

times their spatial structure is indistinguishable from the normal mode (figure 4). The straight line on figure 6(*c*) corresponds to the energy growth of an initial perturbation of unit energy entirely in the most unstable normal mode. Asymptotically it is about a factor of 5 smaller than the maximum possible energy growth of non-modal perturbations with the same α and ϵ or the overall optimal perturbations.

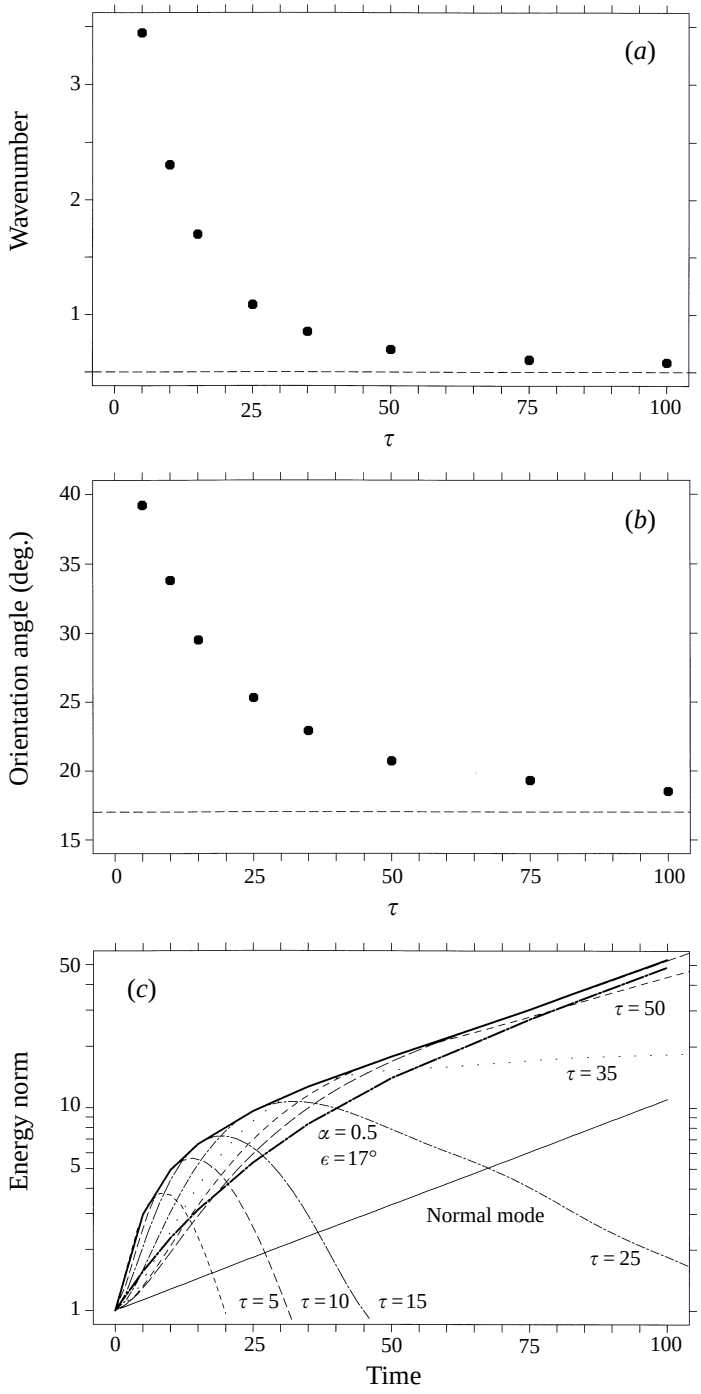

FIGURE 6. Change in (*a*) wavenumber, (*b*) orientation angle and (*c*) maximum possible energy norm as a function of time interval, τ, for $Re = 500$. The dashed lines on (*a*) and (*b*) mark the conditions of the most unstable discrete normal mode. Included on (*c*) is the maximum possible energy growth curve for non-modal perturbations for $\alpha = 0.5$ and $\epsilon = 17°$, and the energy norm as a function of time for the initial condition of unit energy in the unstable discrete normal mode (straight line). Individual growth rate curves corresponding to the optimal initial conditions for $\tau = 5$, 10, 15, 25, 35, 50 and 75 are included.

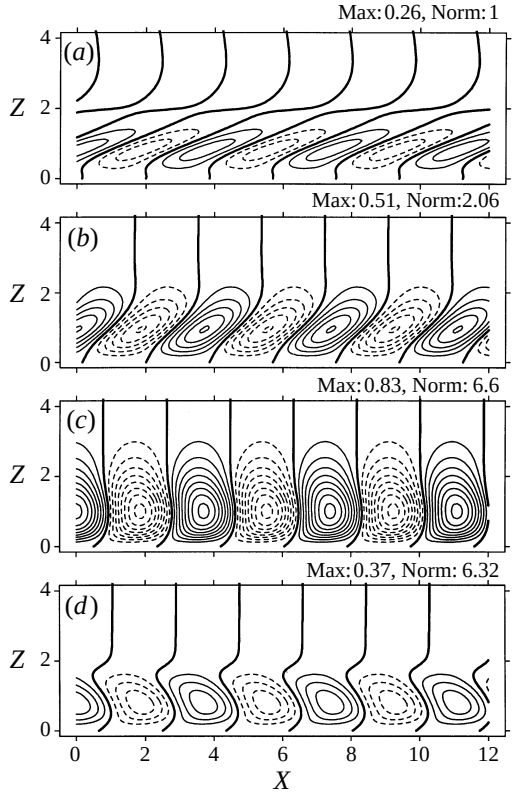

FIGURE 7. Contours of the streamfunction in the plane normal to the roll axis for the $\tau = 15$ optimal perturbation at (*a*) $t = 0$, (*b*) $t = 5$, (*c*) $t = 15$, and (*d*) $t = 25$. The wavenumber is 1.700 and the orientation angle is 29.5° from the surface isobars. The contour interval is 0.1 for all times. Solid contours are positive values and dashed contours are negative. The heavy solid lines mark the zero contour.

3.2. *Evolution of the optimal perturbations*

The evolution of the perturbations is very similar for all of the evanescent instabilities ($\tau < 30$) and for the growing instabilities ($\tau > 30$). We will focus on the $\tau = 15$ optimal perturbation as an example of an evanescent instability and the $\tau = 75$ optimal as a typical growing instability. The wavelength of the $\tau = 75$ instability is about 2.8 times larger than the $\tau = 15$ instability and is oriented at an angle of 19.3° from the surface isobars compared to 29.5° for the $\tau = 15$ perturbation.

3.2.1. *Evanescent instability*: $\tau = 15$

The overturning (u, w) roll motion is best visualized using contour plots of the streamfunction in the (x, z)-plane normal to the roll axis (figure 7). The initial orientation of the streamfunction is mostly tilted to the right except below $z \sim 0.5$ where it tilts to the left. The perturbation is confined below $z \sim 1.5$ which is where the Ekman layer shear is greatest. This configuration is always against the mean cross-stream shear (figure 1). As it develops, the streamfunction is advected by the mean Ekman layer flow until it is essentially vertically oriented at $t = 15$. At this time the maximum amplitude of the streamfunction has increased by a factor of 3.2 from the initial condition and the streamfunction extends almost twice as high from the surface. The energy norm of the instability continues to increase beyond this time, reaching a

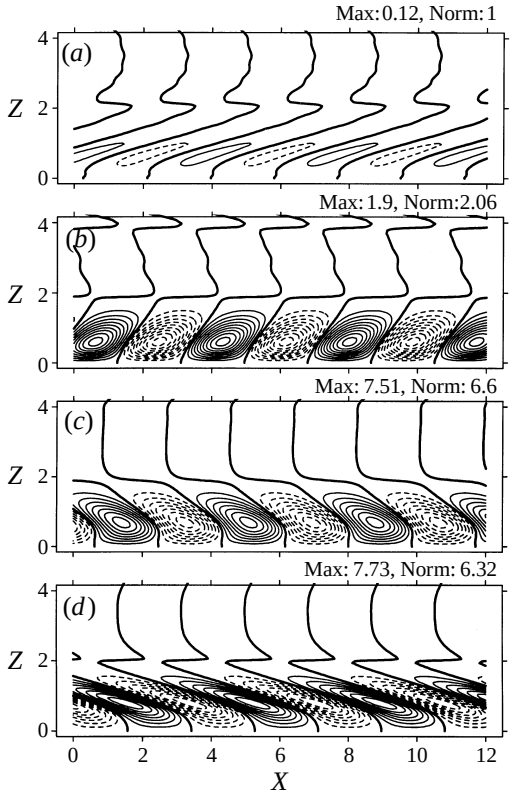

FIGURE 8. Contours of the downstream velocity in the plane normal to the roll axis for the $\tau = 15$ optimal perturbation at (*a*) $t = 0$, (*b*) $t = 5$, (*c*) $t = 15$, and (*d*) $t = 25$. The wavenumber if 1.700 and the orientation angle is 29.5° from the surface isobars. The contour interval is (*a*) 0.1, (*b*) 0.2, (*c*) and (*d*) 1. Solid contours are positive values and dashed contours are negative. The heavy solid lines mark the zero contour.

maximum of 7.23 at $t = 20$. The continued advection by the mean flow ultimately orients the streamfunction mainly along the mean shear by $t = 25$. At this time the maximum amplitude of the streamfunction is only 40 % greater than its initial value.

The axial (v) component of the perturbation follows a strikingly different evolution. Figure 8 shows contours of v in the plane normal to the rolls. Initially there is almost no axial perturbation velocity. However, it is able to exploit the large downstream near-surface mean shear quite effectively so that by $t = 5$ the maximum velocity has increased by a factor of 16. As this velocity increases in magnitude the mean cross-stream flow tilts the v-velocity contours along the mean cross-stream shear. Unlike the overturning flow, the axial perturbation velocity has not yet reached its maximum by $t = 25$ and remains below $z = 2$ throughout its evolution.

3.2.2. *Growing instability*: $\tau = 75$

Qualitatively, the early development of the growing instabilities is very similar to that of the evanescent perturbations. The streamfunction is mostly titled against the mean cross-stream shear at $t = 0$ and is below $z \sim 3$ (figure 9). As it evolves, the streamfunction is sheared by the mean cross-stream flow until its orientation is more upright by $t = 25$. However, the contribution to the perturbation from the unstable normal mode begins to dominate by $t \sim 45$ and the perturbation is indistinguishable

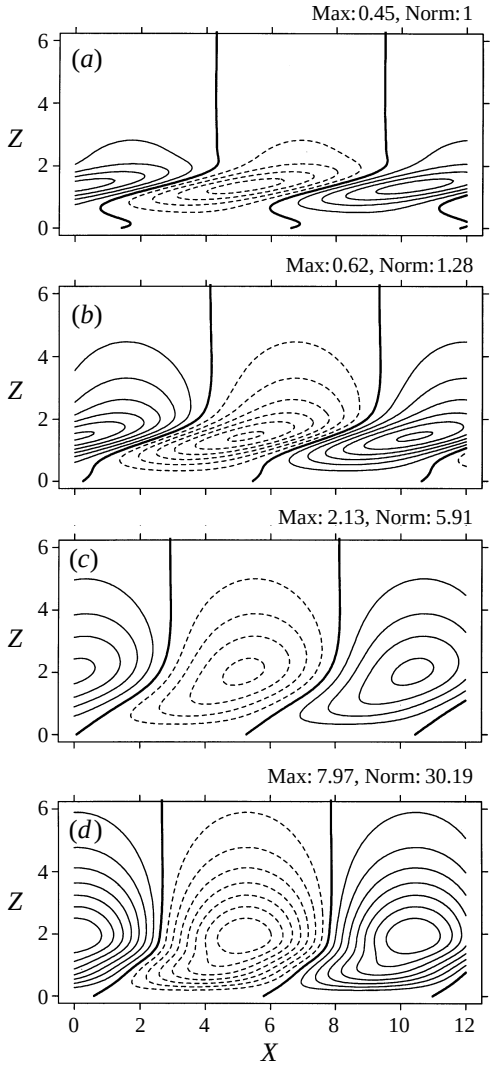

FIGURE 9. Contours of the streamfunction in the plane normal to the roll axis for the $\tau = 75$ optimal perturbation at (*a*) $t = 0$, (*b*) $t = 5$, (*c*) $t = 25$, and (*d*) $t = 75$. The wavenumber if 0.605 and the orientation angle is 19.3° from the surface isobars. The contour interval is: (*a*) and (*b*) 0.1, (*c*) 0.5 and (*d*) 1. Solid contours are positive values and dashed contours are negative. The heavy solid lines mark the zero contour.

from the pure normal mode at $t = 75$. Because of this, the streamfunctions for the growing instabilities never tilt along the mean cross-stream shear. Once in the normal-mode shape, the overturning motion extends vertically to $z \sim 6$.

The axial perturbation velocity is shown in figure 10. As for the $\tau = 15$ optimal perturbation, it is initially almost non-existent, but increases by a factor of 10 in only 5 time units. The mean cross-stream shear tilts the axial velocity towards the left as the perturbation evolves towards its final normal-mode shape which is roughly aligned with the mean cross-stream flow. At all times the perturbation axial velocity is confined below $z \sim 2$.

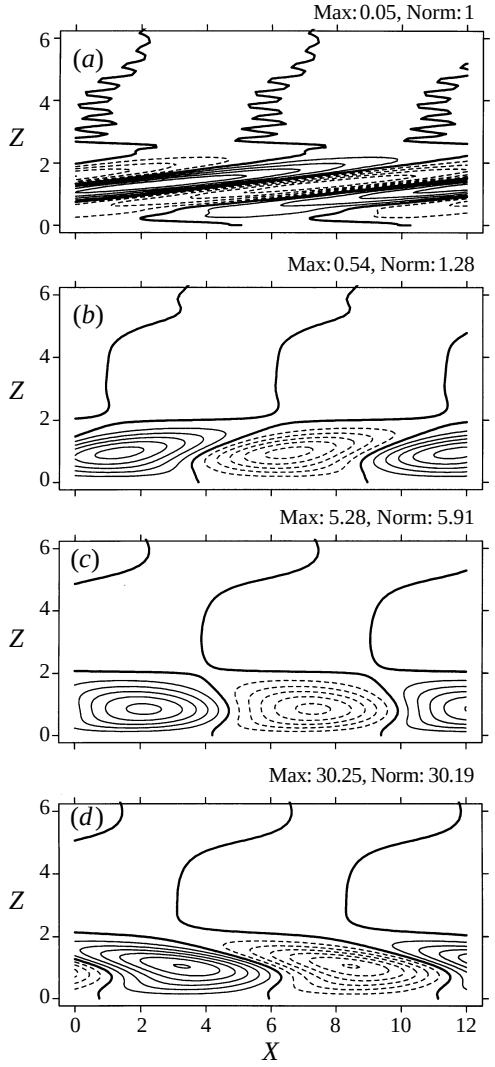

FIGURE 10. Contours of the downstream velocity in the plane normal to the roll axis for the $\tau = 75$ optimal perturbation at (*a*) $t = 0$, (*b*) $t = 5$, (*c*) $t = 25$, and (*d*) $t = 75$. The wavenumber is 0.605 and the orientation angle is 19.3° from the surface isobars. The contour interval is (*a*) 0.01, (*b*) 0.1, (*c*) 1, and (*d*) 5. Solid contours are positive values and dashed contours are negative. The heavy solid lines mark the zero contour.

4. Energetics of the non-modal perturbations

The kinetic energy budget of these linear instabilities can be usefully separated into the contributions from the overturning (OT) and the downstream (DS) motions. These two budgets are linked through the Coriolis redistribution term which, at $Re = 500$, is much weaker than all of the other terms in the budget. The two kinetic energy budgets are

$$\frac{\mathrm{d}k_{OT}}{\mathrm{d}t} = \frac{1}{2}\frac{\partial}{\partial t}(\overline{u^2} + \overline{w^2}) = -\overline{uw}\frac{\mathrm{d}U}{\mathrm{d}z} + \frac{1}{Ro}\overline{uv} - \frac{\partial}{\partial z}\overline{pw} + \frac{1}{Re}\frac{\partial}{\partial z}[\overline{uu}_z + \overline{ww}_z]$$

$$-\frac{1}{Re}[\overline{u_z^2} + \overline{w_z^2} + \alpha^2(\overline{u^2} + \overline{w^2})], \tag{4.1}$$

$$\frac{\mathrm{d}k_{DS}}{\mathrm{d}t} = \frac{1}{2}\frac{\partial}{\partial t}\overline{v^2} = -\overline{vw}\frac{\mathrm{d}V}{\mathrm{d}z} - \frac{1}{Ro}\overline{uv} + \frac{1}{Re}\frac{\partial}{\partial z}[\overline{vv_z}] - \frac{1}{Re}[\overline{v_z^2} + \alpha^2\overline{v^2}], \tag{4.2}$$

where the averages are taken over a wavelength of the perturbation. The first two terms on the right-hand sides of (4.1)–(4.2) are the shear production and Coriolis redistribution terms and the last two terms are the diffusion and dissipation terms. The overturning motions are coupled through the perturbation pressure, whose net effect appears as a vertical pressure diffusion term in (4.1). All of the terms in these budgets are calculated directly from the spectral solution as functions of time and height.

While the vertical energy budget profiles provide insight into the physical process that are affecting the perturbations at any given time, when the budget terms are integrated over all z, we get a clearer picture of how the fluxes from each term contribute to the growth or decay of the instability as a function of time. The integrals of the pressure transport and diffusion terms vanish due to the homogenous boundary conditions. These results are shown in figure 11 for the optimal perturbations for $\tau =$ 15 and 75.

4.1. *Evanescent instability*: $\tau = 15$

The initial OT shear production is positive at all heights with a maximum near $z = 1$. At this height the diffusion, pressure diffusion and dissipation largely balance the shear production and the OT kinetic energy growth rate is slightly negative. The diffusion terms transport the energy due to the shear production away from this level and act as energy sources below $z \sim 0.5$ and above $z \sim 1$ resulting in a net positive OT kinetic energy growth. While in the growing phase as mean advection and pressure diffusion tilt the streamfunction towards a more upright orientation the OT dissipation and diffusion terms become less important at mid-levels and are largest near the surface. The OT shear production at mid-levels remains relatively large. It is offset partially by the pressure diffusion term, but the OT kinetic energy growth rate is still significant. The pressure diffusion continues to transport the energy gained from shear production at mid-levels to the upper and lower layers in the PBL. By $t = 15$, the OT shear production is mostly positive below $z \sim 1$ and negative above so that the total contribution is near zero. The OT dissipation term remains significant and the kinetic energy growth rate turns negative. At later times, while the streamfunction is decaying and is aligned mainly along the mean shear, the OT shear production is mostly negative; OT kinetic energy is returning to the mean flow.

Initially the DS shear production is the only relatively large right-hand-side budget term and the main balance is between it and the DS kinetic energy growth rate. This explains the rapid initial growth of the DS velocity. By $t = 5$, all terms in the DS energy budget greatly exceed those from the OT budget. The DS dissipation and diffusion terms remain almost negligible compared to the shear production so the DS kinetic energy growth rate remains quite large. The DS dissipation term grows steadily and by $t = 15$ is a significant contribution to the budget with a maximum at $z \sim 1$. By $t = 25$, the DS dissipation has increased sufficiently that it is the dominant term in the budget. The DS shear production is negative near the surface and positive above $z \sim 0.5$. At this time both the OT and DS kinetic energy growth rates are negative and the instability is decaying.

In general, the OT kinetic energy growth rate in the evanescent instabilities begins to decay before the time for which the perturbation is an optimal. The OT component of the growth rate is usually negative when $t = \tau$ and the shear production turns negative soon after. The DS shear production remains mostly positive for $t > \tau$. The

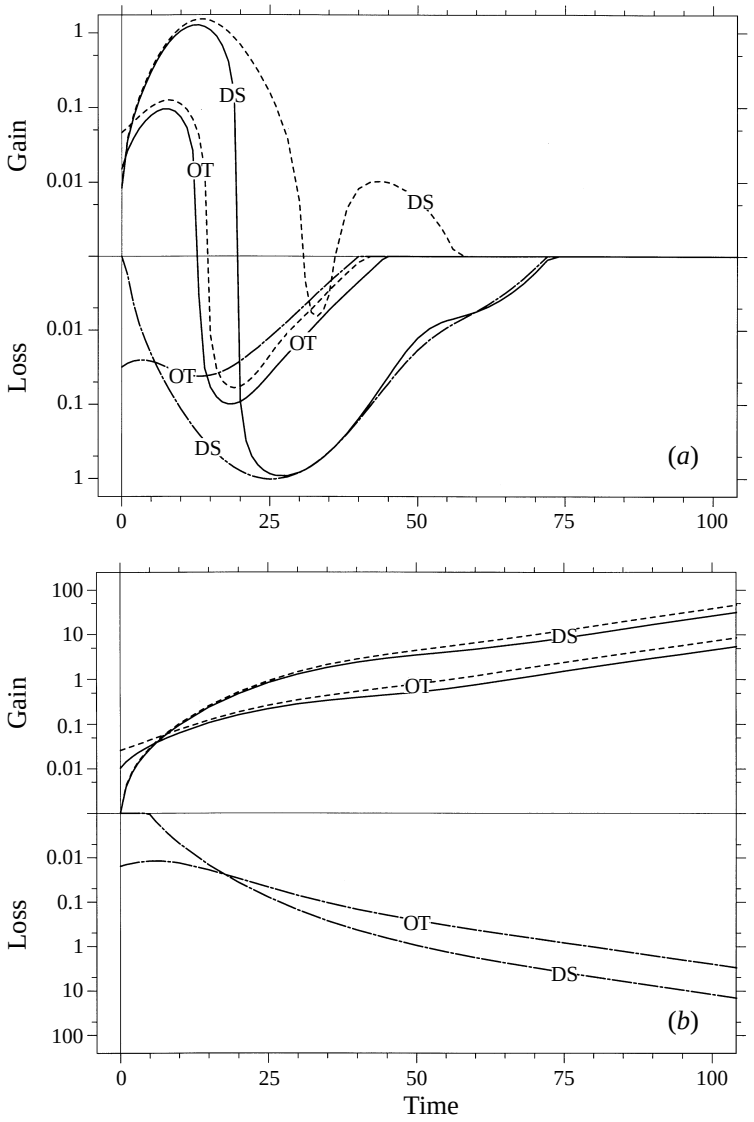

FIGURE 11. Vertically integrated kinetic energy budget terms as a function of time for the (*a*) $\tau = 15$ and (*b*) $\tau = 75$ optimal perturbations. The Coriolis terms cancel between the overturning (OT) and downstream (DS) budget terms and are omitted for clarity. The plotted terms are: energy growth, solid; shear production, dashed; dissipation, dash-dot.

change in sign of the DS growth rate beyond $t = \tau$ is due to the eventual domination of the dissipation over the shear production.

4.2. *Growing instability*: $\tau = 75$

The initial OT kinetic energy budget for the $\tau = 75$ optimal perturbation is very similar to that for $\tau = 15$. In contrast the DS kinetic energy growth rate is initially negative near the surface and positive above. By $t = 5$ the DS shear production is comparable to that of the OT motion. These budgets develop in a manner similar to those of the evanescent instabilities until the contribution of the unstable normal mode begins to dominate. Although the normal-mode instability is much less efficient than the optimal

perturbation at extracting energy from the mean flow at early times, its modal shape is quite effective at maximizing the difference between shear production and dissipation once the transient growth phase has passed. This is the case by $t > 50$. Both the DS and OT shear production rates are positive at all heights while the dissipation rates remain relatively smaller.

5. Discussion

Neutral stratification allows significant simplifications and provides a good base from which more elaborate studies may be performed. Insight into the dynamics of PBL flows that are of practical interest can be obtained from the current results. For example, the polar PBL is often neutrally stratified and the PBL over the oceans is generally near-neutrally stratified (slightly unstable). Data are scarce in both of these regions and PBL parameterizations are heavily relied upon to provide boundary layer winds and fluxes. Improvement of these parameterizations is a priority in both operational and climatological research. However, the PBL is very complex and a more general analysis could include, for example, the effects of surface heat fluxes, variable stratification and baroclinic forcing from large-scale horizontal temperature gradients.

Many numerical modellers have searched for Ekman layer rolls in three-dimensional simulations of the PBL (e.g. Deardorff 1972; Mason and Thomson, 1987; Coleman, Ferziger & Spalart 1992, 1994; Chlond 1992; Moeng & Sullivan 1994). It is very difficult to determine eddy Reynolds numbers of LES calculations equivalent to the definition used in this paper although they are assumed to be in the range from 300 to 1000. The turbulent eddy structure and flux profiles are dependent on the resolution and domain sizes (which are at most marginally capable of capturing the PBL rolls) so LES results cannot be considered conclusive. In general, the neutrally stratified calculations do not generate rolls, although they frequently develop near-surface transient streaks or a statistical 'stretching' of the near-surface longitudinal eddies. Rolls are typically realized when a moderate amount of surface heating is included. The contention is that the purely shear-induced modal instability produces only a very weak finite perturbation that is strengthened by buoyant forcing and then organizes the turbulent eddies.

Deardorff (1972) finds transient near-surface streaks in his neutral LES simulations whose structure does not agree with the predictions of roll characteristics based on normal-mode calculations. The lifetime of a typical streak is 0.1 to $0.2\,f^{-1}$. Rolls are found in slightly and in moderately unstable stratification with wavelengths about 1.5 to 2 times those of the streaks. Mason & Thomson (1987) do not find rolls in any of their neutrally stratified LES simulations. However, they do find that the turbulent eddies near the surface, whose scale and orientation varied with resolution and domain size, are elongated in the direction of the mean shear. Coleman *et al.* (1992, 1994) do not find rolls in their DNS simulations of the neutrally stratified Ekman layer at $Re = 400$, but do simulate them when a moderate amount of surface heating is included. The neutrally stratified case shows elongation of the near-surface eddies. Chlond (1992) performs an LES simulation of a cold air outbreak. In this case surface heat fluxes are important and the boundary layer deepens during the simulation. Early in the simulation he finds small-scale rolls that last about an hour before breaking up. Later on the flow reorganizes into more standard PBL rolls. The evanescent rolls are at an angle of about 50° to the geostrophic wind while those that appear later on are oriented approximately along the geostrophic wind. The ratio of the roll wavelength to PBL depth is 2.6 for the evanescent rolls and 4 for the later rolls. Moeng & Sullivan (1994)

generate small-scale transient streaks oriented at about 30° to the geostrophic wind in their neutrally stratified LES calculation. In slightly unstable stratification, they find organized roll eddies aligned along the geostrophic wind. The wavelength of the equilibrium rolls is about three times that of the streaks.

These numerical results show that evanescent non-model perturbations appear in numerical simulations of the PBL. None of the LES calculations start from a pure Ekman mean flow, so only a qualitative comparison is possible. The data in table 1 show that the maximum relative increase in energy norm between the optimal perturbation and the optimal perturbation constrained to project onto the most unstable normal mode occurs for $\tau = 10$. The orientation of these perturbations from geostrophic ($Re = 150, 500, 1000$) is (20°, 34°, 40°) and the wavelength is (2.9, 4.6, 5.8) times smaller than the predicted roll wavelength. The approximate durations of these optimal perturbations are $(0.4, 0.12, 0.06)\, f^{-1}$. These characteristics qualitatively agree with the characteristics of the streaks in the numerical simulations.

The origin and dynamics of near-wall streaks is a classic problem in fluid mechanics and many different theories have been proposed. Benney & Gustavsson (1981) show that significant transient growth can occur for three-dimensional weakly nonlinear instabilities for which the eigenvalues of the vertical velocity and normal vorticity modes are equal (resonance). Butler & Farrell (1992), Henningson & Schmid (1992) and Reddy & Henningson (1993) show that exact or near resonance is not necessary to generate transient streaks. Comparable energy growth to that found for resonant conditions is found for linear optimal perturbations at neighbouring parameter values for which the resonance mechanism is inoperative. Normal-mode instabilities can often achieve unstable equilibrium or quasi-equilibrium states at subcritical *Re*. This periodic mean flow can then be unstable to three-dimensional secondary instabilities with large growth rates (Orszag & Patera 1983). Butler & Farrell (1994) show that two-dimensional optimal perturbations grow rapidly via linear down-gradient transport of horizontal momentum to reach quasi-equilibrium states more rapidly and with much lower initial energy than the normal modes used in Orszag & Patera (1983). These quasi-equilibria meet a criterion for secondary instability.

Linear mechanisms are as necessary as nonlinear effects to perturbation growth. This has been shown using the Reynolds–Orr equation by Reddy & Henningson (1993), Schmid & Henningson (1994) and Henningson (1996). Hamilton, Kim & Walefe (1995) propose a cycle in which advection of mean momentum by streamwise vortices generates near-surface streaks. These streaks break down due to secondary instability. During this breakdown, nonlinear effects couple energy into linear instability modes in the form of streamwise vortices completing the cycle. Schmid & Henningson (1992) demonstrate that nonlinear effects couple energy into certain modes which grow rapidly through linear mechanisms. This linear growth is limited by nonlinear effects, including mean flow modification. Butler & Farrell (1994) find a similar reduction in the energy growth of optimal perturbations as they reach finite amplitude. Walefe (1995) has argued that this nonlinear reduction in energy growth calls into question the importance of optimal perturbations. Henningson (1996) points out that the nonlinear reduction is like that experienced by normal modes as they approach equilibrium states (e.g. Herbert 1983) and that it does not prohibit the initially linear instability from transferring energy into other scales or from developing secondary instability. Butler & Farrell (1993) demonstrate that the transient streak spacing in wall-bounded turbulent flows is consistent with the optimal perturbations that experience the maximum growth over an eddy turnover time.

The fact that the optimal perturbation analysis predicts a wide variety of large-scale

instabilities, both evanescent and growing, in addition to the normal modes associated with PBL rolls is the important result of this study. That the structure and evolution of the evanescent optimal perturbations are similar to the LES streaks is significant. The evanescent optimal perturbations could generate, through nonlinear effects not calculated in this model, mean flow modifications in the form of transient streaks with associated non-local momentum transport. Such effects are not included in the single-point closure PBL models currently in use in large-scale atmospheric models. It is possible that these nonlinear streaks could also preclude or inhibit the development of equilibrium PBL rolls. However, this hypothesis needs further investigation.

6. Conclusions

The non-modal analyses show that both evanescent and growing optimal perturbations can form in the Ekman layer. These optimal perturbations consist of a near-surface vortex with very weak axial velocity. Because the dissipation in the axial velocity component is initially quite small, the downstream velocity increases rapidly and the perturbation is transformed into a near-surface streak with weaker overturning flow. The important difference between the evanescent and growing perturbations is whether or not they have an initial projection onto an unstable normal mode. The evanescent perturbations are of smaller scale and are oriented at larger angles to the surface isobars then the growing instabilities. The evanescent perturbations cause the maximum possible energy growth over shorter time intervals and require a more rapid initial energy growth. Thus, they are concentrated in the high-shear region near the boundary and are consequently of smaller scale. They are oriented at larger angles to the surface isobars because there is more cross-stream shear for the overturning flow to exploit. The scale, orientation and duration of the evanescent optimal perturbations are in broad agreement with those of the near-surface streaks often found in LES simulations of the neutrally stratified PBL. In these simulations equilibrium PBL rolls are not realized even though the nonlinear stability theory (Foster 1996) predicts they should. There is a strong possibility that the LES streaks are associated with non-modal perturbations and that these perturbations preclude the development of rolls from the normal modes in these simulations.

The author is grateful to Peter Schmid for his courtesy and generosity with his time spent in discussing the theory of optimal perturbations and stability problems in general. Conversations with Hugh Rand, Christopher Bretherton, Jim Barnard and Jim Riley were of great assistance. Thanks also to Robert Brown for his input and support. The comments of the anonymous reviewers led to an improved presentation of these results. This research was supported by NASA support for NSCAT under JPL contract No. 957648, WETNET NAGW-3647 and Radarsat NAGW-4973.

REFERENCES

Alpers, W. & Brummer, B. 1994 Atmospheric boundary layer rolls observed by the synthetic aperture radar aboard the ERS-1 satellite. *J. Geophys. Res.* **99**, 12613–12621.

Anderson, E., Bai, Z., Bischof, C. *et al.* 1992 *LAPACK Users Guide*. SIAM, Philadelphia.

Benney, D. J. & Gustavsson, L. H. 1981 A new mechanism for linear and nonlinear hydrodynamic instability. *Stud. Appl. Maths* **64**, 185–209.

Brown, R. A. 1970 A secondary flow model for the planetary boundary layer. *J. Atmos. Sci.* **27**, 742–757.

Brown, R. A. 1972 On the inflection point instability of a stratified Ekman boundary layer. *J. Atmos. Sci.* **29**, 850–859.

Brown, R. A. 1980 Longitudinal instabilities and secondary flows in the planetary boundary layer: a review. *Rev. Geophys. Space Phys.* **18**, 683–697.

Brown, R. A. 1981 On the use of exchange coefficients in modelling turbulent flow. *Boundary-Layer Met.* **20**, 111–116.

Brown, R. A. & Foster, R. C. 1994 On PBL models for general circulation models. *Global Atmos.-Ocean Syst.* **2**, 163–183.

Butler, K. M. & Farrell, B. F. 1992 Three-dimensional optimal perturbations in viscous shear flow. *Phys. Fluids* A **4**, 1637–1650.

Butler, K. M. & Farrell, B. F. 1993 Optimal perturbations and streak spacing in wall-bounded turbulent shear flow. *Phys. Fluids* A **5**, 774–777.

Butler, K. M. & Farrell, B. F. 1994 Nonlinear equilibration of two-dimensional optimal perturbations in viscous shear flow. *Phys Fluids* **6**, 2011–2020.

Chlond, A. 1992 Three dimensional simulation of cloud street development during a cold-air outbreak. *Boundary Layer Met.* **58**, 161–200.

Coleman, G. N., Ferziger, J. H. & Spalart, P. R. 1990 A numerical study of the turbulent Ekman layer. *J. Fluid Mech.* **213**, 313–348.

Coleman, G. N., Ferziger, J. H. & Spalart, P. R. 1994 A numerical study of the convective boundary layer. *Boundary Layer Met.* **70**, 247–272.

Deardorff, J. W. 1972 Numerical investigation of neutral and unstable planetary boundary layers. *J. Atmos. Sci.* **29**, 91–115.

Etling, D. 1971 The stability of an Ekman boundary flow as influenced by thermal stratification. *Beitr. Phys. Atmos.* **44**, 168–186.

Etling, D. & Brown, R. A. 1993 Roll vortices in the planetary boundary layer: a review. *Boundary-Layer Met.* **65**, 215–248.

Faller, A. J. 1965 Large eddies in the atmospheric boundary layer and their possible role in the formation of cloud rows. *J. Atmos. Sci.* **22**, 176–184.

Faller, A. J. & Kaylor, R. E. 1966 A numerical study of the laminar Ekman layer. *J. Atmos. Sci.* **23**, 466–480.

Farrell, B. F. 1988 Optimal excitation of perturbations in viscous shear flow. *Phys. Fluids* **31**, 2093–2102.

Foster, R. C. 1995 Stability of the stratified, baroclinic Ekman layer. *11th Symp. on Boundary Layers and Turbulence, March 27–31, Charlotte, North Carolina.* AMS.

Foster, R. C. 1996 An analytic model for planetary boundary layer roll vortices. PhD thesis, University of Washington, Seattle.

Gerling, T. W. 1986 Structure of the surface wind fields from the Seasat SAR. *J. Geophys. Res.* **91**, 2308–2320.

Golub, G. H. & Loan C. F. van. 1983 *Matrix Computations.* Johns Hopkins University Press.

Grosch, C. E. & Salwen, H. 1978 The continuous spectrum of the Orr–Sommerfeld equation. Part 1. The spectrum and eigenfunctions. *J. Fluid Mech.* **87**, 33–54.

Haack, T. & Shirer, H. N. 1992 Mixed convective-dynamic roll vortices and their effects on initial wind and temperature profiles. *J. Atmos. Sci.* **49**, 1181–1201.

Hamilton, J. M., Kim, J. & Walefe, F. 1995 Regeneration mechanisms of near-wall turbulence structures. *J. Fluid Mech.* **287**, 317–348.

Henningson, D. 1996 Comment on 'Transition in shear flows. Nonlinear normality versus nonnormal linearity'. *Phys. Fluids* **8**, 2257–2258.

Henningson, D. & Schmid, P. J. 1992 Vector eigenfunction expansions for plane channel flows. *Stud. Appl. Maths* **87**, 15–43.

Herbert, T. W. 1983 On perturbation methods in nonlinear stability theory. *J. Fluid Mech.* **126**, 167–186.

Kaylor, R. E. & Faller, A. J. 1972 Instability of the stratified Ekman boundary layer and the generation of internal waves. *J. Atmos. Sci.* **29**, 497–509.

Leibovich, S. & Lele, S. K. 1985 The influence of the horizontal component of the earth's angular velocity on the stability of the Ekman layer. *J. Fluid Mech.* **150**, 41–87.

Lilly, D. K. 1966 Instability of Ekman boundary flow. *J. Atmos. Sci.* **23**, 481–494.

Mason, P. J. & Thomson, D. J. 1987 Large-eddy simulations of the neutral-state-stability planetary boundary layer. *Q. J. R. Met. Soc.* **113**, 413–443.

MATLAB *Users Guide* 1992 The Mathworks Inc., Natick, MA.

Moeng, C. H. & Sullivan, P. P. 1994 A comparison of shear- and buoyancy-driven planetary boundary layers flows. *J. Atmos. Sci.* **51**, 999–1022.

Mourad, P. D. & Brown, R. A. 1990 On multiscale large eddy states in weakly stratified planetary boundary layers. *J. Atmos. Sci.* **47**, 414–438.

Mourad, P. D. & Walter, B. A. 1996 Viewing a cold air outbreak using satellite-based synthetic aperture radar and advanced very high resolution radiometer imagery. *J Geophys. Res.* **101**, 16391–16400.

Orszag, S. A. & Patera, A. T. 1983 Secondary instability of wall-bounded shear flows. *J. Fluid Mech.* **128**, 347–385.

Reddy, S. C. & Henningson, D. S. 1993 Energy growth in viscous channel flow. *J. Fluid Mech.* **252**, 209–238.

Reddy, S. C., Schmid, P. J. & Henningson, D. S. 1993 Pseudospectra of the Orr–Sommerfeld operator. *SIAM J. Appl. Maths* **53**, 15–47.

Schmid, P. J. & Henningson, D. S. 1992 A new mechanism for rapid transition involving a pair of oblique waves. *Phys. Fluids* A **4**, 1986–1989.

Schmid, P. J. & Henningson, D. S. 1994 Optimal energy density growth in Hagen–Poiseuille flow. *J. Fluid Mech.* **277**, 197–225.

Sorbjan, Z. 1989 *Structure of the Atmospheric Boundary Layer*. Prentice Hall.

Spalart, P. R., Moser, R. D. & Rogers, M. M. 1991 Spectral methods for the Navier–Stokes equations with one infinite and two periodic directions. *J. Comput. Phys.* **96**, 297–324.

Thomson, T. W., Liu, W. T. & Weissman, D. E. 1983 Synthetic aperture radar observation of ocean roughness from rolls in an unstable marine boundary layer. *Geophys. Res. Lett.* **12**, 1172–1175.

Trefethen, L. N. 1992 Pseudospectra of matrices. In *Numerical Analysis* 1991 (ed. D. F. Griffiths & G. A. Watson). Longman.

Trefethen, L. N., Trefethen, A. E., Reddy, S. C. & Driscoll, T. A. 1993 Hydrodynamic stability without eigenvalues. *Science* **261**, 578–584.

Walefe, F. 1995 Transition in shear flows: non-linear normality versus non-normal linearity. *Phys. Fluids* **7**, 3060–3066.